ARTICLE

Direct observation of the double-layering quantized growth of mica-confined ionic liquids

Bingchen Wang,[a] and Lei Li *[a]

Since the interface between ionic liquids (ILs) and solids always plays a critical role in important applications such as coating, lubrication, energy storage and catalysis, it is essential to uncover the molecular structure and dynamics of ILs confined to solid surfaces. Here, we report direct observation of a unique double-layering quantized growth of three IL (i.e., [Emim][FAP], [Bmim][FAP] and [Hmim][FAP]) nanofilms on mica. AFM results show that the IL nanofilms initially grow only by covering more surface areas at the constant film thickness of 2 monolayers (ML) until a quantized increase in the film thickness by another 2 ML. Based on the AFM results, we propose a double-layering model describing the molecular structure of IL cations and anions on the mica surface. The interesting double-layering structure can be explained as the result of several competing interactions at the IL-mica interface. Meanwhile, the time-dependent AFM results indicate that the topography of IL nanofilms could change with time and mobility of the nanofilm is lower for ILs with longer alkyl chains, which can be attributed to the more ordered packing between longer alkyl chains. The findings here have important implications on the molecular structure and dynamics of ILs confined to solid surfaces.

Introduction

Ionic liquids (ILs) have drawn more and more research interests because of their extraordinary physiochemical properties. Unlike common inorganic salts, the liquid phase is thermodynamically favorable for ILs under ambient conditions, since the Coulombic attractions are disrupted due to the bulky and asymmetric organic cations and anions.[1-3] Their excellent properties, including high thermal stability, wide liquidus range, negligible volatility, excellent solvating capability,[4-6] make them ideal candidates for applications in separations, chemical synthesis, etc.[7-11] The interface between ILs and solids is especially crucial to many promising applications, such as electrolytes for energy storage devices,[12, 13] lubricants for nano- and microelectromechanical systems (NEMS/MEMS) and hard disk drives (HDD),[14-18] absorbents for carbon capture,[19, 20] and green catalysis.[21, 22] As a result, it is critical to understand the molecular structure of ILs confined to solid surfaces. Muscovite mica has been frequently used as the model solid because of its atomically smooth surface and well-studied surface chemistry.[23, 24] Muscovite mica exhibits layered structure along the (001) basal plane, with interlayered K+ between two aluminosilicate layers to balance the negatively charged

crystals.[23] Upon cleavage at the interlayer, statistically equal amounts of K+ are distributed on both mica surfaces.[25]

Molecular liquids form solid-like layering when confined on atomically flat solid surfaces as ultrathin films.[26-28] For example, when absorbed on the mica surface, water molecules have been found to form ~0.2nm-thick icelike monolayers and then icelike bilayers at higher relative humidity (RH) due to the hydrogen bonding.[25, 29-32] Similarly, as two mica surfaces approach each other at the molecular scale when immersed in nonpolar liquids, oscillatory functions of force to separation distances can be detected, corresponding to discrete monolayers of the nonpolar liquids.[33, 34] For molecularly thin perfluoropolyether (PFPE) films confined on amorphous nitrogenated carbon, complete wetting has been observed below the film thickness of one monolayer, while dewetting becomes overwhelming as the film grows thicker than one monolayer because of the favorable boding within the PFPE molecules over the solid/liquid interaction.[16, 35] When surfactant molecules (e.g., quaternary ammonium surfactants) in aqueous solutions below the critical micelle concentrations (CMC) are adsorbed on solid surfaces, they generally form monolayers or spherical aggregates, whereas the cationic surfactant molecules above CMC form the thermodynamically favorable wormlike aggregates in full-cylinders on the hydrophilic mica surfaces and half-cylinders on the hydrophobic graphite surfaces.[36-38] Similar to molecular liquids, ILs have been found to form solid-like layering structures when confined to the mica surface.[24] Atkin et al. performed the AFM force-distance study with a tip approaching and leaving the mica surface in two protic ILs, EAN and PAN, and an aprotic [Emim][Ac], and concluded that ILs form solid-like extended layering structure on mica.[3, 39, 40] Perkin et al. used surface force apparatus (SFA) to study the oscillation

distance from the squeeze-out of an ion pair for $[C_nMIm][NTf_2]$ between two mica sheets.[41-43] They proposed that the ILs with shorter alkyl chains form monolayers of cations/anions with the alkyl chains parallel to mica, while the ILs with longer alkyl chains form tail-to-tail bilayer aggregation with the alkyl chains perpendicular to mica. Moreover, they measured the friction by shearing two mica sheets with nanometer-thick ILs confined in between using SFA.[44, 45] Quantized friction regimes were observed at various loads, which correspond to different layers of ions after squeeze-out. Espinosa-Marzal et al. also observed the oscillatory structural forces with reducing separation distances and an irreversible solid-like structural change for $[Hmim][EtSO_4]$ under nanoconfinement using extended SFA, which supports the possible IL layering with the cation alkyl chain normal to the surface.[46, 47] Gebbie et al. performed force-distance measurements across $[C_nmim][NTf_2]$ (n=2-4) and proposed that ILs screen charged solid surfaces by forming short-range Stern layers and long-range diffuse double layers, where the near-surface nanostructure can extend up to 3 nm away from the solid surfaces.[48-50] In AFM force-distance and SFA studies, the molecular structure was indirectly characterized by deciphering the force-distance and the friction-load profiles. Liu et al. noticed the coexistence of the liquid phase and the stable solid-like phase of $[Bmim][PF_6]$ on the mica surface at room temperature (RT) under tapping mode AFM.[51] In contrast, Bovio et al. reported that there is only solid-like layering for $[Bmim][NTf_2]$ on mica.[52] Later, Yokota et al. detected inhomogeneous layering structures of $[Bmim][NTf_2]$ and $[Bmim][BF_4]$ at the IL/mica interface using frequency-modulation AFM (FM-AFM).[53] While the previous works showed the extended layering structure of ILs on the mica surface, a complete picture of the interfacial structure of IL cations and anions at the molecular level has not yet been uncovered.

In this study, the interfacial molecular structures of mica-confined ILs with various alkyl chain lengths in the cations, i.e., [Emim][FAP], [Bmim][FAP], and [Hmim][FAP], were investigated by AFM. Unlike the solid-confined molecular liquids and surfactants, it was directly observed that the IL nanofilms grow in a quantized way on mica by the thickness of ~2 ML. A double-layering interfacial molecular model of IL cations and anions on the mica surface has been proposed based on the equilibrium nanofilm topographies. Time-dependent AFM results have showed the slower spreading for ILs with longer alkyl chains when confined to the mica surface, which can be attributed to the more ordered packing between longer alkyl chains.

Results and discussion

Quantized growth of [Emim][FAP] on mica

When confined to a solid surface, ILs often form interfacial molecular structures dramatically different from the bulk structure.[6, 43, 54] In the current study, a quantized double-layering growth of [Emim][FAP] nanofilms was directly observed in the AFM results at RH higher than 30%. The growth of the nanofilms was controlled by sequentially increasing the concentration of the IL solutions during thin film fabrications, and the surface characterizations were performed within half an hour after the thin film fabrications. Initially, the IL film only covers more solid surface areas at the constant film thickness. At a critical stage of film growth, there is a sharp increase in the overall film thickness by ~2ML. The nanofilm thickness remains constant again afterward as the IL film grows. The film thickness was taken as the average distance between the top of the film and the mica surface for each film growth stage.

As shown in Fig. 1a-c, when fabricated from solutions at lower concentrations, i.e., 0.25 g/L to 0.75 g/L, the thickness of [Emim][FAP] nanofilms remains constant at ~1.8 nm. As the nanofilm grows, the IL films only cover more solid surface areas at this stage. The film topography changes from small islands to more closely packed islands, and then to connected sponges. Interestingly, when the IL concentration increased from 0.75 g/L to 1 g/L, a quantized increase in the thickness of the sponge-like nanofilm to ~4.4 nm was observed, as seen in Fig. 1d. As the concentration increased from 1 g/L to 1.5 g/L, the overall thickness of the growing IL nanofilms remained at ~3.5 nm (Fig. 1e). However, the film topography switches to one loosely connected film sitting on another smooth film upon the film growth. The thicknesses of the top and bottom layers are ~1.6 nm and ~1.8 nm, respectively.

If the [Emim][FAP] molecules in bulk are assumed to be cubes, the edge length can be calculated by $(\frac{M/N_A}{\rho})^{\frac{1}{3}}$, where ρ is the bulk density (1.71 g/cm³ at RT), M is the molecular weight (556.17 g/mol), and N_A is the Avogadro constant.[16, 55] The edge length of [Emim][FAP] molecules is calculated as 0.81 nm, which is roughly half of the thickness of [Emim][FAP] nanofilms fabricated from low concentrations. Assuming one monolayer (ML) of the IL nanofilm is one layer of [Emim][FAP] molecules densely packed in the lateral direction, the starting thickness of [Emim][FAP] nanofilms is the thickness of ~2 ML. Interestingly, the film thicknesses did not grow consecutively with the increasing concentration of the IL solutions. Instead, the thicknesses increased by ~2 ML from 0.75 g/L to 1 g/L. Except for the quantized increase, the film thickness remained constant at ~2 ML for thinner films and ~4 ML for thicker films.
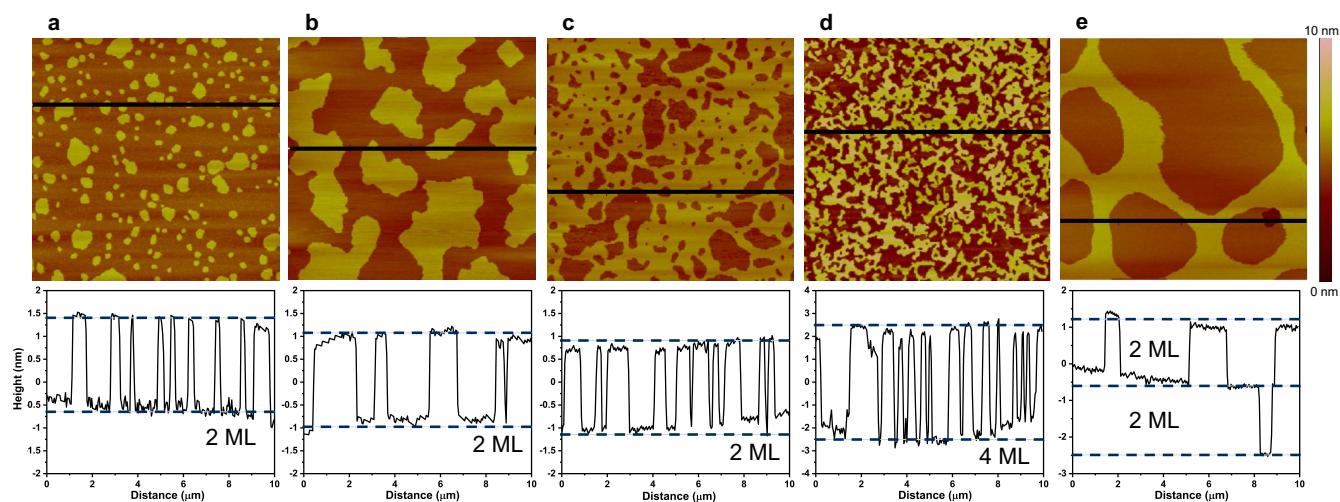
Fig. 1 AFM images and their corresponding line profiles of mica-confined [Emim][FAP] fabricated from the concentration of (a) 0.25 g/L (30% RH), (b) 0.5 g/L (34% RH), (c) 0.75 g/L (52% RH), (d) 1 g/L (52% RH), and (e) 1.5 g/L (34% RH). The AFM scan areas are 10 μm by 10 μm, and the inset scale bar is for the z-direction. The x-axis and y-axis for the line profiles are the distance along the cut in the horizontal direction (μm) and the height in the vertical direction (nm), respectively.

Fig. 2 AFM images and their corresponding line profiles of mica-confined [Bmim][FAP] fabricated from the concentration of (a) 0.25 g/L (31% RH), (b) 0.75 g/L (43% RH), (c) 1 g/L (31% RH), (d) 1.5 g/L (55% RH), and (e) 2 g/L (43% RH). The AFM scan areas are 10 μm by 10 μm, and the inset scale bar is for the z-direction. The x-axis and y-axis for the line profiles are the distance along the cut in the horizontal direction (μm) and the height in the vertical direction (nm), respectively.
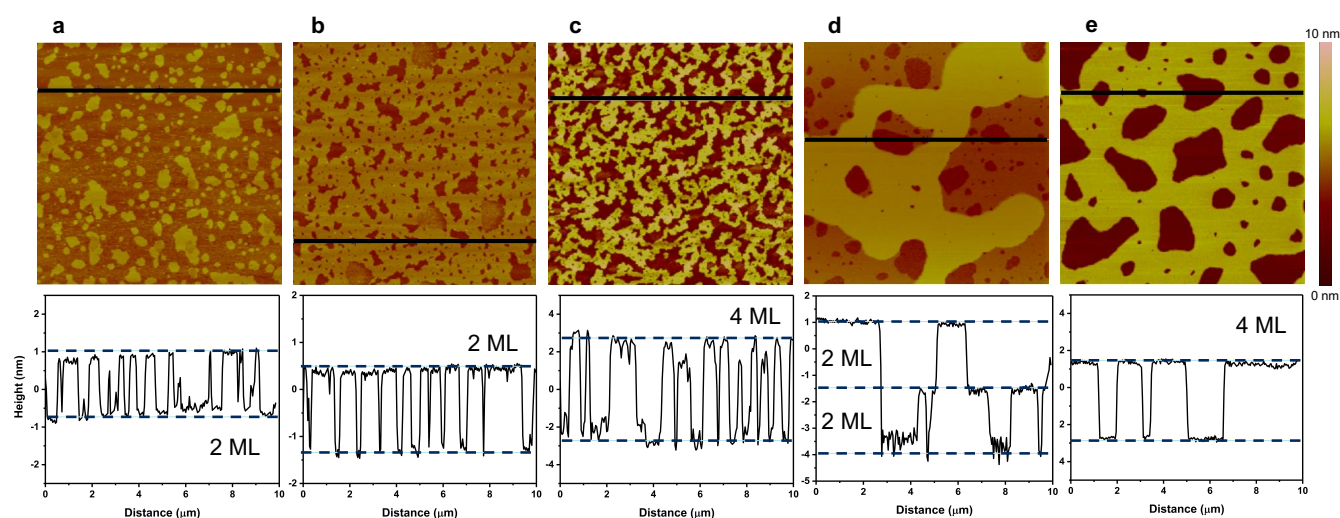
Fig. 3 AFM images and their corresponding line profiles of mica-confined [Hmim][FAP] fabricated from the concentration of (a) 0.25 g/L (30-47% RH), (b) 0.5 g/L (34-47% RH), (c) 0.75 g/L (30-47% RH), and (d) 1 g/L (34-47% RH). For each concentration, the scan was taken within 0.5 hour and after 1 week after the sample fabrication. The AFM scan areas are 10 μm by 10 μm, and the inset scale bar is for the z-direction. The x-axis and y-axis for the line profiles are the distance along the cut in the horizontal direction (μm) and the height in the vertical direction (nm), respectively.
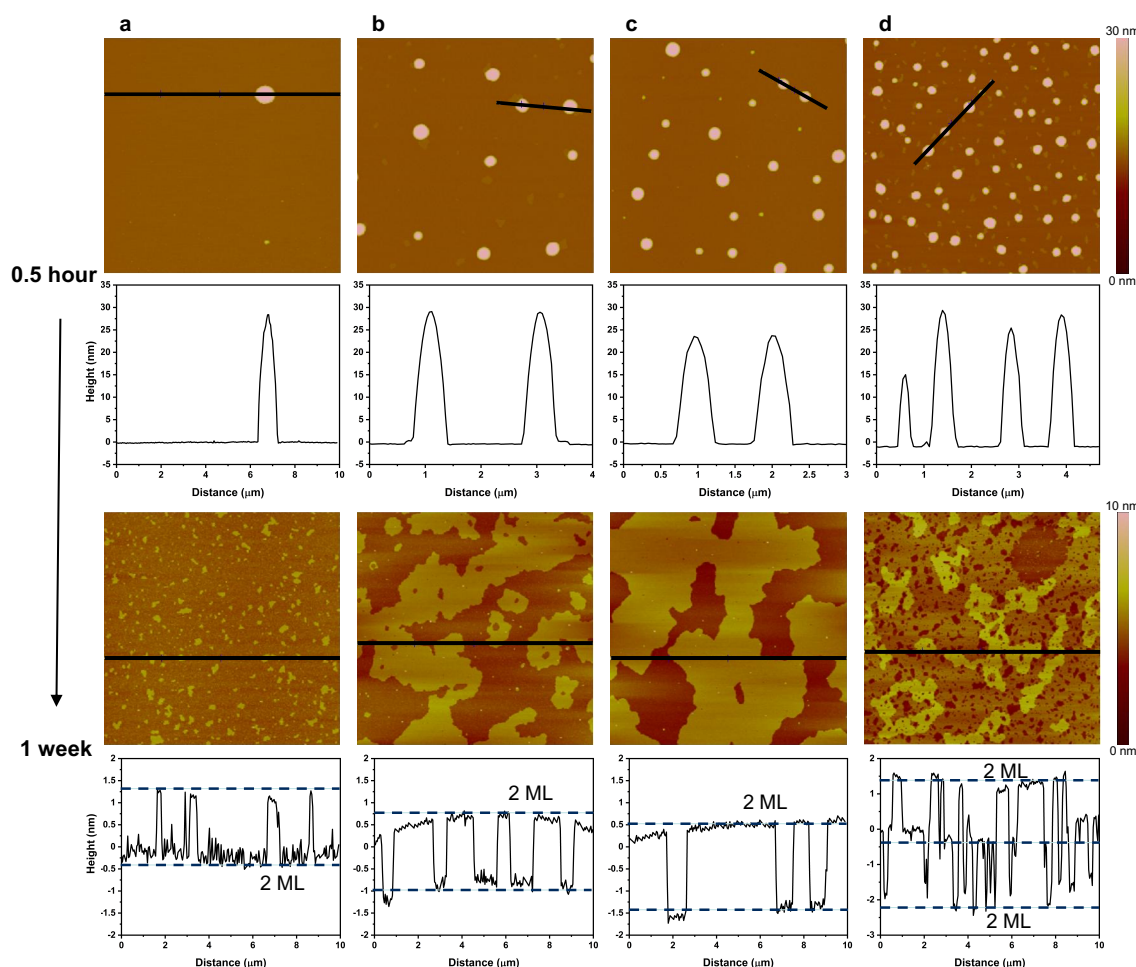
Double-layering interfacial molecular structure

Similar to the quantized growth of [Emim][FAP] nanofilms, the nanofilms of [Bmim][FAP], which has a longer alkyl chain in the imidazolium cation, also exhibit quantized growth on the mica surface at RH higher than 30%. The AFM images and the line profiles in Fig. 2 show the quantized growth of mica-confined [Bmim][FAP]. The edge length of the [Bmim][FAP] molecule is estimated to be 0.84 nm based on its bulk density of 1.63 g/cm³ at RT and its molecular weight of 584.23 g/mol. When the solution concentrations are low, i.e., from 0.25 g/L to 0.75 g/L (Fig. 2a-b), the film thickness remains constant at ~1.5-1.7 nm that is the thickness of ~2ML. As the nanofilm grows, it only covers more solid surface areas, with the islands growing bigger and bigger until they are connected. Similar to the growth of [Emim][FAP], as the concentration increases from 0.75 g/L to 1 g/L, the [Bmim][FAP] nanofilm on mica stops growing with the film thickness constant at ~2 ML thick. Instead, a quantized growth in the film thickness from ~1.7 nm to ~4.4 nm was observed (Fig. 2c). The increase in the film thickness is again about the thickness of 2 ML. The overall thickness remains at

~4.4-4.6 nm for the nanofilms of [Bmim][FAP] fabricated from the concentration of 1 g/L to 1.5 g/L (Fig. 2c-d). During this stage of film growth, the overall film thickness remained at ~4 ML thick, similar to the [Emim][FAP] nanofilms at this stage. Upon the growth of the films, [Bmim][FAP] covers more mica surfaces to form smoother nanofilms. For the nanofilm fabricated from the concentration of 1.5 g/L (Fig. 2d), the film topography again switches to one film with a thickness of ~2.4 nm sitting on another smooth film with a thickness of ~2.2 nm. The thicknesses of both layers are ~2 ML thick. As the dipcoating concentration increases to 2 g/L, the top layer grows in full, resulting in one smooth film on the solid surface. The film thickness is ~4.1 nm, which is about the thickness of 4 ML.

The growth of [Hmim][FAP], which has the longest alkyl chain in the cation among the three ILs, acts very differently from the other two ILs on mica under RH higher than 30%. Instead of the layering structures, [Hmim][FAP] forms nanodroplet structures when confined on the mica surface as nanofilms. As shown in Fig. 3a, when the nanofilm was initially fabricated from the most dilute solution (0.25 g/L), one nanodroplet with a height of ~30 nm and a diameter of ~1 nm was observed within the scan area

at the initial state (within half an hour after dipcoating). As the [Hmim][FAP] nanofilm grows (Fig. 3b-d), the density of the IL nanodroplets becomes higher and higher at the initial states, which is again very different from the quantized growth of layers of [Emim][FAP] and [Bmim][FAP]. No layering structure was observed at all for all stages of film growth.

Table 1 Surface tension values of the ILs at RT.

	Surface tension [mN/m]
[Emim][FAP]	34.3 ± 0.08
[Bmim][FAP]	32.3 ± 0.07
[Hmim][FAP]	31.5 ± 0.05

The surface tension results of three ILs measured by the pendant drop analysis are shown in Table 1. The results are also consistent with previous reports.[56, 57] There is an inverse correlation between the measured surface tension and the alkyl chain length of the cations. Almeida et al.[58] and Zhou et al.[59] concluded that the longer alkyl chain leads to the lower surface tension because the stronger steric effect between ions with longer alkyl chains induces the lower electrostatic interaction. Kolbeck et al.[60] and Pensado et al.[61] proposed that the nonpolar alkyl chains prefer to orient toward air at the liquid-air interface for ILs with longer alkyl chains, which results in the lower surface tension. Our results show that the nanofilms of [Emim][FAP] and [Bmim][FAP], which have ethyl chains and butyl chains in the cations, respectively, exhibit the layering structures on mica, and the growth of the layers is discontinuous. However, the nanofilms of [Hmim][FAP], which has the longest hexyl chain in the cations and the lowest surface tension, show the nanodroplet structures on mica. Based on Young's equation,[62] a liquid with lower surface tension is expected to have better wettability on a solid surface. However, the nanoscopic wettability of [Hmim][FAP] with the lowest surface tension is the lowest among the three ILs on mica. The nanoscopic structures of solid-confined ILs are very different from the bulk structures of ILs on solids.[3, 63] For ILs confined to the mica surface, it is expected that there is a competition between the solid/liquid interaction and the liquid/liquid interaction. Previous ATR-FTIR and AFM results suggest that water absorbed on the mica surface from ambient humidity dissolves and mobilizes the surface K^+, as water has a high dielectric constant.[64, 65] At the solid/liquid interface, ion exchange between the IL cations and K^+ is thus enabled, and layered packing of ILs could be initiated. As a result, layering structures were observed for the nanofilms of [Emim][FAP] and [Bmim][FAP] under RH > 30%. However, [Hmim][FAP] has a longer C_6 alkyl chain in the cation than [Emim][FAP] and [Bmim][FAP]. The stronger solvophobic force results in more ordered nanostructure and enhances the cohesive interaction within the IL, so nanodroplet structures were observed for the [Hmim][FAP] nanofilms as a result of the strong liquid/liquid cohesion. Similar differences in the interfacial structures between imidazolium ILs with C_6 alkyl chains and imidazolium ILs with shorter alkyl chains were also reported based on the AFM force measurement results.[66, 67] [Hmim][FAP] on both highly ordered pyrolytic graphite (HOPG) and Au(111) was found to have stronger interfacial structures against the push-through force than [Emim][FAP], because the longer cation alkyl chain leads to enhanced solvophobic interaction.

Interestingly, after the films sit for 1 week under the RH higher than 30%, layering structures were again observed for mica-confined [Hmim][FAP] at various stages of film growth, i.e., nanofilms fabricated from the concentration of 0.25 g/L, 0.5 g/L, 0.75 g/L, and 1 g/L. As shown in Fig. 3, the molecular structures of the series of [Hmim][FAP] nanofilms after 1 week were very similar to the quantized layering structures of the nanofilms of [Emim][FAP] and [Bmim][FAP] within half an hour after the thin film fabrications. Only layering structure of [Hmim][FAP] were observed, while no nanodroplets remained on the mica surface anymore. The edge length of the cubic [Hmim][FAP] molecule is estimated to be 0.87 nm based on its bulk density of 1.56 g/cm^3 at RT and its molecular weight of 612.28 g/mol. For nanofilms fabricated from the concentration of 0.25 g/L, 0.5 g/L, and 0.75 g/L after 1 week, the nanodroplets spread into layers with film thicknesses ~1.5-1.8 nm of ~2 ML, equal to the thickness of ~2ML. The film morphology changes from spikes to more connected islands. As the concentration increases from 0.75 g/L to 1 g/L, another layer with a thickness of ~2 ML grows on the bottom layer. A quantized increase in the overall film thickness from ~2 ML to ~4 ML (~3.3 nm) was again observed. These findings imply that the alkyl chain length in the IL cations may have little impact on the equilibrium states of the morphology of the IL nanofilms confined on mica, while the spreading kinetics of the IL films could vary significantly with the change of alkyl chain length.

The above-discussed AFM results provide the key information to uncover the molecular structure of IL cations and anions on mica. By comparing the film thicknesses of the three ILs at the equilibrium states, it is evident that their equilibrium ML thicknesses are almost the same. For instance, the thicknesses of the IL nanofilms right before the quantized growths, i.e., 0.75 g/L [Emim][FAP] (Fig. 1c), 0.75 g/L [Bmim][FAP] (Fig. 2b), and 0.75 g/L [Hmim][FAP] (Fig. 3c), are ~1.8 nm, ~1.7 nm, and ~1.8 nm, respectively. The chemical structures of the three cations with various alkyl chain lengths and the [FAP] anion are presented in Fig. S1. As listed by the detailed dimensions, there is an increase in the alkyl chain length by 0.25 nm for the transitions from C_2 to C_4 and from C_4 to C_6. Consequently, the very similar ML thicknesses of various ILs determined by AFM imply that the alkyl chains are parallel rather than perpendicular to the solid surface. Additionally, the molecular arrangement is not likely to be one layer of cations adjacent to the mica surface that occupy the empty spots left by the dissociated K^+ and one layer of anions on top of the cation layer to form one ML altogether, because this model does not explain why the thinnest nanofilm is ~2 ML thick and why the quantized film growth is always by ~2 ML. Here, based on the directly-observed thickness results from AFM, we propose a double-layering interfacial molecular model of IL cations and anions when confined to the mica surface, as shown in Fig. 4 with [Bmim][FAP] on mica as an example. Within the double-layer building block, adjacent to the mica surface is a layer of cations, which results from the attractive electrostatic force between

the negatively charged mica surface and the IL cation. The imidazolium rings are oriented perpendicular to mica, which is also suggested by previous density-functional theory (DFT) and molecular dynamics (MD) simulation works,[68-70] and the alkyl chains are oriented parallel to the mica surface. Adjacent to the first cation layer is another layer of cations. The configuration is similar to the first cation layer, i.e., the imidazolium rings perpendicular and the alkyl chains parallel to the mica surface. The nonpolar alkyl chains in the first and second cation layers closely pack with each other orderly due to the solvophobic interaction, and the polar imidazolium heads are far away from each other due to the repulsive electrostatic force. Two [FAP] anions sit on top of the two cations. The electrostatic interaction drives the phosphorous atom of the anion to be close to the CH between the methyl and the butyl chains of the imidazolium ring (C(2)H), as indicated by previous ab initio molecular orbital calculations.[71-75] Besides, as also shown in Fig. 4, the cations in the next building block at the back closely pack with the cations in the front building block due to the π-π stacking interaction between the imidazolium rings.[43, 63, 76] The negative charge density on the fresh mica surface after K^+ are dissolved by absorbed water is approximately one per 0.47 nm^2 on average.[23, 49, 77] After the surface K^+ are dissociated by the absorbed water from mica, the IL cations need to occupy the empty spots left by the K^+, which initiates the layering of IL cations and anions.[64] The relatively small K^+ reside within the vacancy of the layers to preserve the electroneutrality of the IL nanofilm system, including negatively charged mica surface, dissociated K^+, and two pairs of ions. Taking into consideration the area covered by the standing cation and the separation distance of π-π stacking between two blocks, the mica surface area covered by one IL building block is approximately the same as the area of one negative charge that is created by the

dissociation of K^+. The sizes of two cations (~0.5 nm each) and one anion (~0.7 nm) in the z-direction account for the overall thickness of a building block. As a result, the thickness of the double-layering molecular structure of the IL nanofilms is ~1.7 nm (Fig. 4), which is consistent with the AFM results.

While the double-layering molecular model describes the structure of [Emim][FAP], [Bmim][FAP] and [Hmim][FAP] on mica, one needs to be careful in generalizing the conclusion here. Since the double-layering model results from the competition among several interactions, e.g., electrostatic interaction between mica and cation, electrostatic interaction between cation and anion, solvophobic interaction, and it depends on the exact structure of ILs and solids, it is likely the molecular structure will change for different ILs and solids. In the current study, the thicknesses of the first double-layer and the second double-layer are not always exactly the same. The electrostatic force at the interface of IL and mica is strong to induce more ordered molecular arrangements in the first double-layer than in the second double-layer, which may lead to a difference in the thicknesses.[41] Indeed, the findings here indicate the complexity of the molecular structure of solid-confined ILs.

Different spreading kinetics of ILs on mica

Our AFM results showed that the alkyl chain length in the IL cations has little impact on the nanofilm morphology on mica under equilibrium states. However, AFM results also suggest that the spreading of the [Hmim][FAP] nanofilms is the slowest among the three ILs. Therefore, the effect of the alkyl chain length in the IL cations on the spreading kinetics of mica-confined ILs has also been investigated.
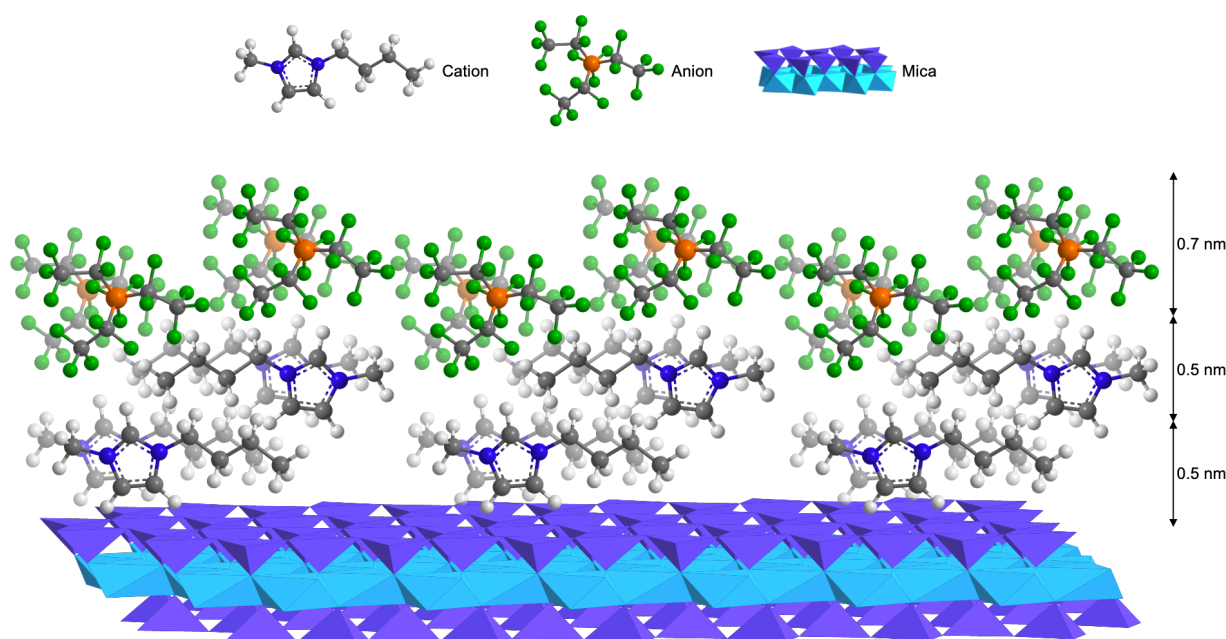

Fig. 4 Double-layering molecular model of [Bmim][FAP] on the mica surface

[Emim][FAP], [Bmim][FAP], and [Hmim][FAP] nanofilms were fabricated using the same solution concentration of 0.75 g/L and the topography of the nanofilms were compared with respect to the lead time after the thin film fabrication. The films were fabricated, characterized, and stored under the RH lower than 20% during the entire experimental period. While absorbed water forms large island-like films to full monolayers at RH > 30% that is expected to increase the mobility of K⁺ and thus promote the spreading of IL nanofilms, only small and isolated two-dimensional clusters can be formed on the mica surface at RH < 20%.[23, 25, 29, 78] As a result, the spreading of IL nanofilms is expected to be slower when RH is lower than 20%, and the chance to capture the nanodroplets becomes higher. This idea was also supported by a previous report that the initial molecular structure of [Bmim][FAP] gradually changes from extended layers to droplets with decreasing RH.[64] In light of this, it is expected that the IL film morphology at the initial stages could change from extended layering at RH > 30% to nanodroplets at RH < 20%. Accordingly, RH < 20% was chosen here to maximize the chance of capturing the spreading process during the transition from nanodroplets to solid-like layers.

The AFM images and the corresponding line profiles in Fig. S4 show the time-dependent nanofilm morphology of [Emim][FAP] fabricated from the concentration of 0.75 g/L under RH < 20%. The nanofilm behaves as sponge-like layering at the initial state (within half an hour after thin film fabrication), same as the morphology under RH > 30%. The results indicate that the spreading process for the [Emim][FAP] nanofilm is very fast after dipcoating, so only layering structure was observed within the experiment time scale. No change of the molecular structure over time was observed, and the RMS surface roughness values remain almost the same at various lead time (Table 2). The molecular structure remained as sponge-like layering, and the nanofilm thickness was constant at ~2 ML for up to one week.

Table 2 RMS surface roughness results of the three IL nanofilms fabricated from 0.75 g/L solutions at various lead time

	[Emim][FAP]	[Bmim][FAP]	[Hmim][FAP]
0.5 hour	0.496 nm	2.44 nm	7.01 nm
0.5 day	0.588 nm	2.16 nm	9.03 nm
2 days	0.794 nm	1.54 nm	4.13 nm
1 week	0.826 nm	0.897 nm	1.49 nm
3 weeks			0.608 nm

As expected, a combination of nanodroplets and layering with heights of up to ~10 nm was observed at the initial state for the [Bmim][FAP] nanofilm fabricated from the concentration of 0.75 g/L (Fig. 5a). The nanodroplet structure at the initial state under RH < 20% is very different from the sponge-like layering under RH > 30%. The existence of nanodroplet suggests that the spreading of [Bmim][FAP] is slower than that of [Emim][FAP]. The nanodroplets spread gradually over time, as indicated by the AFM topography and the RMS surface roughness values. At this stage of isotropic spreading, the height of the nanodroplets decreases over time, and the coverage of the nanofilm on mica increases over time. It is worth noting that when the film thickness is above 4 ML, i.e., after 0.5 hour and 0.5 day, the height of the films at various locations are not uniform anymore, possibly because the layering structure far away from the solid/liquid interface is dampened. The film morphology changes from nanodroplets with irregular shapes to islands with a constant thickness of ~4 ML after 2 days. Eventually, after one week, the islands spread anisotropically to form layering nanofilm with a constant thickness of ~2 ML. The significantly lower mobility and slower spreading of mica-confined [Bmim][FAP] nanodroplets compared to the spreading in macroscale is also analogous to the previous finding.[79]

For the [Hmim][FAP] nanofilm fabricated from the concentration of 0.75 g/L, only nanodroplets with heights up to ~50 nm were observed at the initial state under RH < 20%, as shown in Fig. 5b. The nanodroplets then start to spread isotropically over time to cover more areas on mica. However, the spreading of [Hmim][FAP] nanodroplets is much slower than the spreading of [Bmim][FAP] nanodroplets, as indicated by the comparison of AFM topography in Fig. 5 and the RMS surface roughness values in Table 2 at various lead time. Besides, the solid/liquid contact lines of [Hmim][FAP] nanodroplets are closer to circles than the contact lines of [Bmim][FAP], since the cohesion interaction within the [Hmim][FAP] molecules with C_6 alkyl chain tails dominate over the templating effect at the solid/liquid interface at these stages. After one week, the film morphology slowly changes from nanodroplets to large islands with a constant thickness of ~4 ML. Interestingly, it was noticed that a layer with a thickness of ~2 ML develops under another layer with a thickness of ~2 ML at the edge of an island, as shown in Fig. S5. This phenomenon indicates that the morphology of the [Hmim][FAP] nanofilm after one week is not at its equilibrium state yet, and the nanofilm still has the tendency to continue to spread slowly. Eventually, after three weeks, the islands spread anisotropically to form the layering nanofilm with a constant thickness of ~2 ML.
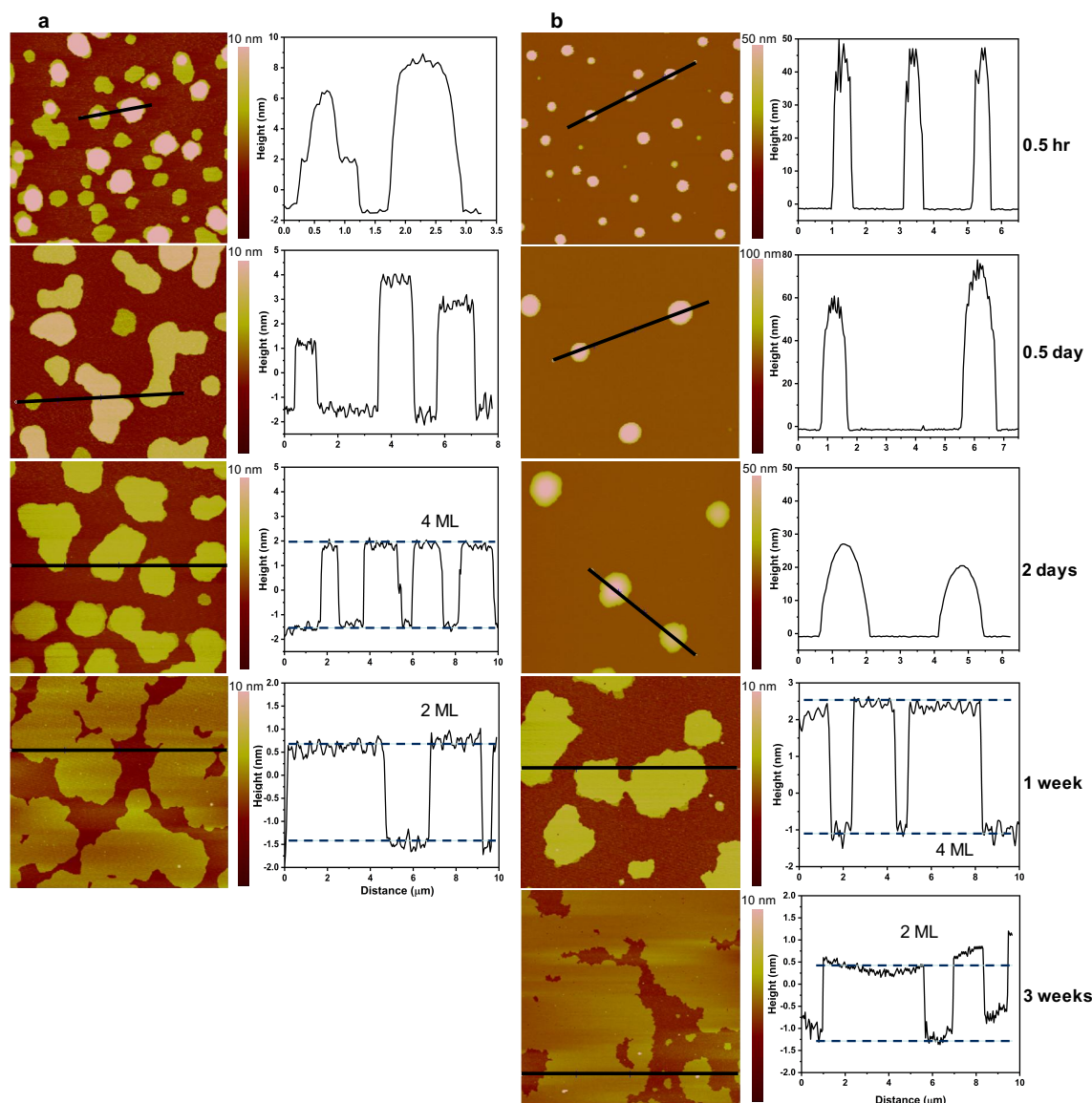
Fig. 5 AFM images and their corresponding line profiles of time-dependent nanofilms of (a) [Bmim][FAP] and (b) [Hmim][FAP] fabricated from the concentration of 0.75 g/L. The ambient RH was 12-20% the whole time. All AFM scan areas are 10 μm by 10 μm, and the inset scale bars are for the z-direction. The x-axis and y-axis for the line profiles are the distance along the cut in the horizontal direction (μm) and the height in the vertical direction (nm), respectively.

The time-dependent AFM results under RH < 20% show a clear dependence of the spreading kinetics of mica-confined ILs on the cation alkyl chain length. The spreading of the nanofilm of [Emim][FAP] that contains the shortest alkyl chain is the fastest among the three IL nanofilms. The solvaphobic interaction within the IL with C_2 alkyl chains is too week to preserve a strong cohesion within the IL molecules, so the solid/liquid interfacial interaction dominates from the beginning. The spreading of the [Bmim][FAP] nanofilm is slower than the [Emim][FAP] nanofilm. A distinct change of surface morphology with lead time, i.e., from the combination of nanodroplets and layering islands after half an hour to smooth layering films after one week, has been observed. The mild solvaphobic interaction of the IL with C_4 alkyl chains is able to compete with the templating effect on the mica

surface, so the mobility of the [Bmim][FAP] nanodroplets is lower than that of [Emim][FAP]. The spreading of the [Hmim][FAP] nanofilm is the slowest among the three IL nanofilms. It takes up to three weeks for the nanofilm to reach its equilibrium state of the smooth layer with the thickness of ~2 ML. As [Hmim][FAP] has the longest C_6 alkyl chain in the cation, the intermolecular cohesion is strong enough to preserve the nanodroplet structure with the shape of a spherical cap for the longest time among the three ILs. When confined as nanofilms, the tendency for ILs with long cation alkyl tail to initially form nanodroplets and then slowly spread is related to the nanostructure in bulk IL. Due to the ion amphiphilicity, bulk IL molecules organize into spatially heterogeneous polar and apolar domains, similar to the

aggregations of traditional surfactants.[3, 6, 80] The solvophobic effect induces the alkyl chains to self-assemble into sponge-like clusters, and the increasing alkyl chain length in the cations drives the formation of more distinct and continuous nanostructures,[5, 81-83] resulting in he initial nanodroplet structure. The competition between the solvophobic interaction within ILs and the templating effect of the mica surface accounts for the slower spreading of ILs with longer alkyl tails and the final layered structrue. The finding here highlights the complexity in determining the molecular structure of solid-confined ILs. Due to the possible time dependence, even the "experimental data" might not be taken as the last word if the time effect is not considered. The time- and RH-dependence also explain the inconsistent results reported previously.

Conclusions

In conclusion, the interfacial molecular structures of mica-confined ILs with various alkyl chain lengths in the cations, i.e., [Emim][FAP], [Bmim][FAP], and [Hmim][FAP], have been systematically investigated by AFM. Double-layering quantized growth of the nanofilms of [Emim][FAP] and [Bmim][FAP] at RH > 30% has been directly observed. Initially, the IL films only cover more solid surface areas at the constant film thickness of 2 ML. Then a quantized increase in the film thickness by 2 ML was observed. The nanofilm thickness remains constant afterward as the nanofilm grows. The AFM thickness results directly indicate that the cation alkyl chain length has no impact on the nanofilm topographies under equilibrium states. Based on the AFM results, we have proposed a double-layering model describing the interfacial molecular structure of IL cations and anions on the mica surface. Within the double-layer building block, the first two layers adjacent to the mica surface are cation layers with the imidazolium rings perpendicular to mica and the closely-packed alkyl tails parallel to mica, and two anions sit on top of the two cations. The structure can be explained by the multiple interactions involved at the IL-mica interface. Meanwhile, the time-dependent AFM results at RH < 20% reveal the effect of the cation alkyl chain length on the spreading kinetics of mica-confined IL nanofilms. The spreading is slower for ILs with longer alkyl chains due to the stronger solvophobic interactions. Our results provide insights into the molecular structure and dynamics of solid-confined ILs.

Experimental

Materials

The imidazolium ILs utilized were a series of hydrophobic ILs with the same [FAP] anions and three different alkyl chain lengths in the cations, i.e., 1-ethyl-3-methylimidazolium tris(pentafluoroethyl)trifluorophosphate ([Emim][FAP]), 1-butyl-3-methylimidazolium tris(pentafluoroethyl)trifluorophosphate ([Bmim][FAP]), and 1-hexyl-3-methylimidazolium tris(pentafluoroethyl)trifluorophosphate ([Hmim][FAP]). They

were acquired from Millipore Sigma and used as received, and the purities are higher than 98%. Their molecular structures are shown in Fig. S1. The solvent for ILs was 2,3-dihydrodecafluoropentane (marketed as Vertrel XF) with high volatility. Vertrel XF was purchased from Fisher Scientific and used as received. Muscovite mica sheets (highest quality grade V1) were purchased from Ted Pella.

Thin film fabrication

Nanometer-thick IL films on mica were fabricated with a KSV Instruments dipcoater based on a previously established approach in our lab.[84, 85] IL solutions were made by dissolving ILs in Vertrel XF at a series of concentrations. Mica sheets were cleaved by a sharp tweezer right before the dipcoating process to make fresh mica surfaces. The AFM image and the corresponding line profile of the atomically smooth mica surface are shown in Fig. S2 as control. The cleaved mica pieces were dipped into and pulled out from the IL solutions at a constant speed of 60 mm/min using the dipcoater, as shown in Fig. S3. The growths of the IL nanofilms in this study were controlled by sequentially increasing the concentrations of the IL solutions.

AFM characterization

The surface topography of the IL nanofilms on mica was characterized by tapping-mode AFM using a Veeco Dimension V Scanning Probe Microscope. The AFM probe used (MikroMasch NSC14/AL BS) has an 8 nm aluminum tip on an n-type silicon cantilever, a resonance frequency of 160 kHz, and a force constant of 5.0 N/m. The scan area was set at 10 μm by 10 μm with a pixel density of 256 by 256, so the lateral resolution was 39 nm.

Surface tension measurement

The liquid-air surface tension values of the bulk ILs were measured by the pendant drop analysis with a VCA Optima XE contact angle machine at room temperature.

Author Contributions

B.W. performed the experiments. L.L. conceived and supervised the project. B.W. and L.L. wrote the manuscript. All the authors discussed the data and revised the manuscript.

Conflicts of interest

There are no conflicts to declare.

Acknowledgements

Notes and references

1. I. Krossing, J. M. Slattery, C. Daguenet, P. J. Dyson, A. Oleinikova and H. Weingärtner, *Journal of the American Chemical Society*, 2006, **128**, 13427-13434.
2. X. Gong and L. Li, *Advanced Engineering Materials*, 2018, **20**, 1700617.
3. R. Hayes, G. G. Warr and R. Atkin, *Physical Chemistry Chemical Physics*, 2010, **12**, 1709-1723.
4. Z. Lei, B. Chen, Y.-M. Koo and D. R. MacFarlane, *Chemical Reviews*, 2017, **117**, 6633-6635.
5. S. Zhang, J. Zhang, Y. Zhang and Y. Deng, *Chemical Reviews*, 2017, **117**, 6755-6833.
6. R. Hayes, G. G. Warr and R. Atkin, *Chemical reviews*, 2015, **115**, 6357-6426.
7. N. V. Plechkova and K. R. Seddon, *Chemical Society Reviews*, 2008, **37**, 123-150.
8. L. Lozano, C. Godínez, A. De Los Rios, F. Hernández-Fernández, S. Sánchez-Segado and F. J. Alguacil, *Journal of Membrane Science*, 2011, **376**, 1-14.
9. T. Welton, *Chemical reviews*, 1999, **99**, 2071-2084.
10. J. P. Hallett and T. Welton, *Chemical reviews*, 2011, **111**, 3508-3576.
11. L. Liu, J. Wang, X. Xu and B. Wang, *Journal of Inclusion Phenomena and Macrocyclic Chemistry*, 2014, **80**, 437-441.
12. M. Watanabe, M. L. Thomas, S. Zhang, K. Ueno, T. Yasuda and K. Dokko, *Chemical reviews*, 2017, **117**, 7190-7239.
13. E. Jónsson, *Energy Storage Materials*, 2020, **25**, 827-835.
14. X. Gong, B. West, A. Taylor and L. Li, *Industrial & Engineering Chemistry Research*, 2016, **55**, 6391-6397.
15. F. Zhou, Y. Liang and W. Liu, *Chemical Society Reviews*, 2009, **38**, 2590-2599.
16. B. Wang, C. Moran, D. Lin, H. Tang, E. Gage and L. Li, *ACS Applied Nano Materials*, 2019, **2**, 5260-5265.
17. B. Wang, C. Moran, H. Tang and L. Li, *ACS Applied Nano Materials*, 2020, **3**, 8803-8809.
18. A. C. Lertola, B. Wang and L. Li, *Industrial & Engineering Chemistry Research*, 2018, **57**, 11681-11685.
19. X. Zhang, X. Zhang, H. Dong, Z. Zhao, S. Zhang and Y. Huang, *Energy & Environmental Science*, 2012, **5**, 6668-6681.
20. E. D. Bates, R. D. Mayton, I. Ntai and J. H. Davis, *Journal of the American Chemical Society*, 2002, **124**, 926-927.
21. Q. Zhang, S. Zhang and Y. Deng, *Green Chemistry*, 2011, **13**, 2619-2637.
22. V. I. Pârvulescu and C. Hardacre, *Chemical Reviews*, 2007, **107**, 2615-2665.
23. H. K. Christenson and N. H. Thomson, *Surface Science Reports*, 2016, **71**, 367-390.
24. Y. Wang and L. Li, *Langmuir*, 2020, **36**, 2743-2756.
25. J. Hu, X.-D. Xiao, D. Ogletree and M. Salmeron, *Science*, 1995, **268**, 267-269.
26. S. Granick, *Science*, 1991, **253**, 1374-1379.
27. U. Raviv, P. Laurat and J. Klein, *Nature*, 2001, **413**, 51-54.
28. J. Klein and E. Kumacheva, *Science*, 1995, **269**, 816-819.
29. P. Miranda, L. Xu, Y. Shen and M. Salmeron, *Physical review letters*, 1998, **81**, 5876.
30. A. Verdaguer, G. Sacha, H. Bluhm and M. Salmeron, *Chemical reviews*, 2006, **106**, 1478-1510.
31. H. Bluhm, T. Inoue and M. Salmeron, *Surface science*, 2000, **462**, L599-L602.
32. J. N. Israelachvili and R. M. Pashley, *Nature*, 1983, **306**, 249-250.
33. J. N. Israelachvili, P. M. McGuiggan and A. M. Homola, *Science*, 1988, **240**, 189-191.
34. R. G. Horn and J. N. Israelachvili, *The Journal of Chemical Physics*, 1981, **75**, 1400-1411.
35. R. Waltman, *Langmuir*, 2004, **20**, 3166-3172.
36. I. Grosse and K. Estel, *Colloid and Polymer Science*, 2000, **278**, 1000-1006.
37. P. Kékicheff and C. Contal, *Langmuir*, 2019, **35**, 3087-3107.
38. S. Manne and H. E. Gaub, *Science*, 1995, **270**, 1480-1482.
39. R. Atkin and G. G. Warr, *The Journal of Physical Chemistry C*, 2007, **111**, 5162-5168.
40. D. Wakeham, R. Hayes, G. G. Warr and R. Atkin, *The Journal of Physical Chemistry B*, 2009, **113**, 5961-5966.
41. S. Perkin, L. Crowhurst, H. Niedermeyer, T. Welton, A. M. Smith and N. N. Gosvami, *Chemical Communications*, 2011, **47**, 6572-6574.
42. S. Perkin, *Physical Chemistry Chemical Physics*, 2012, **14**, 5052-5062.
43. A. M. Smith, K. R. Lovelock and S. Perkin, *Faraday discussions*, 2013, **167**, 279-292.
44. A. M. Smith, M. A. Parkes and S. Perkin, *The journal of physical chemistry letters*, 2014, **5**, 4032-4037.
45. A. M. Smith, K. R. Lovelock, N. N. Gosvami, T. Welton and S. Perkin, *Physical Chemistry Chemical Physics*, 2013, **15**, 15317-15320.
46. L. A. Jurado, H. Kim, A. Rossi, A. Arcifa, J. K. Schuh, N. D. Spencer, C. Leal, R. H. Ewoldt and R. M. Espinosa-Marzal, *Physical Chemistry Chemical Physics*, 2016, **18**, 22719-22730.
47. L. A. Jurado, H. Kim, A. Arcifa, A. Rossi, C. Leal, N. D. Spencer and R. M. Espinosa-Marzal, *Physical Chemistry Chemical Physics*, 2015, **17**, 13613-13624.
48. M. A. Gebbie, M. Valtiner, X. Banquy, E. T. Fox, W. A. Henderson and J. N. Israelachvili, *Proceedings of the National Academy of Sciences*, 2013, **110**, 9674-9679.
49. M. A. Gebbie, A. M. Smith, H. A. Dobbs, G. G. Warr, X. Banquy, M. Valtiner, M. W. Rutland, J. N. Israelachvili, S. Perkin and R. Atkin, *Chemical Communications*, 2017, **53**, 1214-1224.
50. M. A. Gebbie, H. A. Dobbs, M. Valtiner and J. N. Israelachvili, *Proceedings of the National Academy of Sciences*, 2015, **112**, 7432-7437.
51. Y. Liu, Y. Zhang, G. Wu and J. Hu, *Journal of the American Chemical Society*, 2006, **128**, 7456-7457.
52. S. Bovio, A. Podesta, C. Lenardi and P. Milani, *The journal of physical chemistry B*, 2009, **113**, 6600-6603.
53. Y. Yokota, T. Harada and K.-i. Fukui, *Chemical communications*, 2010, **46**, 8627-8629.
54. Y.-L. Wang, B. Li, S. Sarman, F. Mocci, Z.-Y. Lu, J. Yuan, A. Laaksonen and M. D. Fayer, *Chemical reviews*, 2020, **120**, 5798-5877.
55. T. Cremer, L. Wibmer, S. K. Calderón, A. Deyko, F. Maier and H.-P. Steinrück, *Physical Chemistry Chemical Physics*, 2012, **14**, 5153-5163.
56. M. Součková, J. Klomfar and J. Pátek, *The Journal of Chemical Thermodynamics*, 2012, **48**, 267-275.
57. Q.-S. Liu, J. Tong, Z.-C. Tan, U. Welz-Biermann and J.-Z. Yang, *Journal of Chemical & Engineering Data*, 2010, **55**, 2586-2589.
58. H. F. Almeida, M. G. Freire, A. M. Fernandes, J. A. Lopes-da-Silva, P. Morgado, K. Shimizu, E. J. Filipe, J. N. Canongia

Lopes, L. M. Santos and J. o. A. Coutinho, *Langmuir*, 2014, **30**, 6408-6418.

59. Z. B. Zhou, H. Matsumoto and K. Tatsumi, *ChemPhysChem*, 2005, **6**, 1324-1332.

60. C. Kolbeck, J. Lehmann, K. Lovelock, T. Cremer, N. Paape, P. Wasserscheid, A. Froba, F. Maier and H.-P. Steinruck, *The Journal of Physical Chemistry B*, 2010, **114**, 17025-17036.

61. A. S. Pensado, M. F. C. Gomes, J. N. C. Lopes, P. Malfreyt and A. A. Pádua, *Physical Chemistry Chemical Physics*, 2011, **13**, 13518-13526.

62. T. Young, *Philosophical transactions of the royal society of London*, 1805, 65-87.

63. X. Gong, A. Kozbial, F. Rose and L. Li, *ACS applied materials & interfaces*, 2015, **7**, 7078-7081.

64. X. Gong, B. Wang, A. Kozbial and L. Li, *Langmuir*, 2018, **34**, 12167-12173.

65. H.-W. Cheng, J.-N. Dienemann, P. Stock, C. Merola, Y.-J. Chen and M. Valtiner, *Scientific reports*, 2016, **6**, 1-9.

66. H. Li, F. Endres and R. Atkin, *Physical Chemistry Chemical Physics*, 2013, **15**, 14624-14633.

67. H. Li, R. J. Wood, F. Endres and R. Atkin, *Journal of Physics: Condensed Matter*, 2014, **26**, 284115.

68. F. Zhang, C. Fang and R. Qiao, *The Journal of Physical Chemistry C*, 2018, **122**, 9035-9045.

69. Y. Yokota, H. Miyamoto, A. Imanishi, K. Inagaki, Y. Morikawa and K.-i. Fukui, *Physical Chemistry Chemical Physics*, 2018, **20**, 6668-6676.

70. S. Kamalakannan, M. Prakash, M. M. Al-Mogren, G. Chambaud and M. Hochlaf, *The Journal of Physical Chemistry C*, 2019, **123**, 15087-15098.

71. S. Watanabe, M. Nakano, K. Miyake, R. Tsuboi and S. Sasaki, *Langmuir*, 2014, **30**, 8078-8084.

72. S. Tsuzuki, H. Tokuda, K. Hayamizu and M. Watanabe, *The Journal of Physical Chemistry B*, 2005, **109**, 16474-16481.

73. S. Tsuzuki, H. Tokuda and M. Mikami, *Physical Chemistry Chemical Physics*, 2007, **9**, 4780-4784.

74. P. A. Hunt, C. R. Ashworth and R. P. Matthews, *Chemical Society Reviews*, 2015, **44**, 1257-1288.

75. E. I. Izgorodina and D. R. MacFarlane, *The Journal of Physical Chemistry B*, 2011, **115**, 14659-14667.

76. F. Tang, T. Ohto, T. Hasegawa, M. Bonn and Y. Nagata, *Physical Chemistry Chemical Physics*, 2017, **19**, 2850-2856.

77. P. J. Sides, D. Faruqui and A. J. Gellman, *Langmuir*, 2009, **25**, 1475-1481.

78. J. Hu, D. Ogletree and M. Salmeron, *Surface science*, 1995, **344**, 221-236.

79. X. Gong, B. Wang and L. Li, *ACS omega*, 2018, **3**, 16398-16402.

80. R. Atkin and G. G. Warr, *The Journal of Physical Chemistry B*, 2008, **112**, 4164-4166.

81. Y. Wang and G. A. Voth, *The Journal of Physical Chemistry B*, 2006, **110**, 18601-18608.

82. S. M. Urahata and M. C. Ribeiro, *The Journal of chemical physics*, 2004, **120**, 1855-1863.

83. J. N. Canongia Lopes and A. A. Padua, *The Journal of Physical Chemistry B*, 2006, **110**, 3330-3335.

84. A. Merzlikine, L. Li, P. M. Jones and Y.-T. Hsia, *Tribology Letters*, 2005, **18**, 279-286.

85. Y. Wang, J. Sun and L. Li, *Langmuir*, 2012, **28**, 6151-6156.

ARTICLE